



# Parametric evaluation and prediction of design parameters of geofoam using artificial neural network and extreme gradient boosting models

Parvathi Geetha Sreekantan<sup>1</sup> · Aali Pant<sup>2</sup> · G. V. Ramana<sup>3</sup>

Received: 12 October 2023 / Accepted: 20 June 2024 / Published online: 1 July 2024  
© Springer Nature Switzerland AG 2024

## Abstract

Expanded polystyrene (EPS) geofoam is increasingly used in the construction industry as a lightweight fill material. The selection of an appropriate grade of geofoam in such cases is dictated by their elastic modulus and compressive strength. However, a comprehensive parametric study on the influencing factors of compression behaviour, which is extremely critical for the design of geofoam, is rarely reported. In the present study, the effect of nominal density, apparent density, strain rate, geometry, and ambient temperature on the elastic modulus, permissible compressive stress, yield stress and compressive strength of geofoam is investigated by conducting a series of uniaxial compression tests. The variation of compressive responses due to each influencing factor is evaluated using scatter matrices and statistical bar plots. Furthermore, results reported in the literature were collated, to develop machine learning based generalised prediction models using Artificial Neural Network and Extreme Gradient Boosting algorithms. The XGBoost models demonstrated superior performance compared to the ANN models, achieving accuracies surpassing 87%. The correlation heat map of the results indicates that the apparent density, size, and ambient temperature control the compressive response of geofoam, while model-dependent feature analysis quantified the relative importance of these parameters. For conservative design and quality assurance, testing a 50 mm geofoam cube at a strain rate of 1% per minute, at the maximum ambient temperature of the construction site is recommended. This study enables the design engineers in the selection of the appropriate grade of geofoam and the associated project cost estimation.

**Keywords** EPS geofoam · Temperature · Density · Size · Artificial neural network · Extreme gradient boosting

## Introduction

Over the last three decades, polymeric foams have been used in the construction industry for various applications such as road embankment filing [1–4], compressible inclusion [5–9], vibration and noise isolation [10–13] and thermal insulation [14–16]. The simplicity, ease and faster pace of construction make it the preferred material for construction, including embankments. These foams are 20–100 times lighter than conventional embankment fill material [17]. Geofoam is a generic term for polymeric foams used in geotechnical engineering applications. Due to its ease of manufacture, Expanded Polystyrene (EPS) foam is the geofoam most commonly used for these applications. As of 2022, EPS geofoam has a global market of USD 900 million in the construction industry and expected an annual growth of 7% [18].

The term “compressive strength” of geofoam is generally attributed to the compressive resistance at 10% strain

---

✉ Parvathi Geetha Sreekantan  
parvathi.crri@nic.in

Aali Pant  
aalipant@iitj.ac.in

G. V. Ramana  
ramana@civil.iitd.ac.in

<sup>1</sup> Geotechnical Engineering Division, CSIR-Central Road Research Institute, New Delhi 110025, India

<sup>2</sup> Civil and Infrastructure Engineering, Indian Institute of Technology Jodhpur, Jodhpur, Jodhpur 342037, India

<sup>3</sup> Department of Civil Engineering, Indian Institute of Technology Delhi, Hauz Khas, New Delhi 110016, India

or yield stress, whichever is lower [19]. However, ASTM D7180 [20] limits the compressive strain of EPS geofoam to 1% for geotechnical applications. Thus, the compressive resistance at 1% strain, which may be termed permissible compressive stress, is the most significant factor governing the design of EPS geofoam in various geotechnical applications. Yield stress and compressive resistance at 10% strain are essential parameters for characterising the plastic response of geofoam. Thus, an initial assessment of these compressive parameters under site-specific conditions will enable the designer to select the geofoam of suitable grade.

Several investigations [21–29] examined the compressive characteristics of EPS geofoam with varying nominal densities, which is referred to the density of blocks obtained during production and post-processing in the industrial stage. However, the compressive responses of the geofoams having the same nominal density, reported by different authors, exhibited a wide variation. However, the actual density, also known as apparent density, may differ from the nominal density, leading to discrepancies in the results. This variation could also be due to other influencing factors such as geometry, ambient temperature, or rate of straining. Several researchers assessed the selective, if not comprehensive, impact of some of these influencing factors on the compressive behaviour of EPS geofoam [30–35]. Nevertheless, there is a scarcity of thorough research that investigates the various factors that influence the compression behaviour of geofoam, a crucial aspect in the design process.

Amongst these parameters, temperature has a significant influence on compression behavior of EPS geofoam. As per Žiliūtė et al. [36], the temperature of the subgrade is typically similar to the ambient temperature. Since the ambient temperature in the Indian subcontinent can often exceed 46 °C [37], a thorough evaluation of the compression behaviour of EPS geofoam under elevated temperatures is necessary to develop suitable design parameters for its application as embankment fill. Zou and Leo [38] investigated the confined compression behaviour at varying temperatures from 23 to 45 °C for EPS geofoam having a nominal density of 20 kg/m<sup>3</sup>. They observed a minor reduction in the initial elastic modulus and compressive response at 10% strain of the specimen. Krundaeva et al. [39] reported a decrease in dynamic compressive strength for elevated temperatures and an increase for subzero temperatures for EPS geofoam with a 10 kg/m<sup>3</sup> nominal density. Based on the literature review, it is observed by the authors that there are limited studies that have been conducted to study the role of ambient temperature on compressive behavior of EPS geofoam.

Of late, researchers have explored the application of machine learning methods to characterise several geomaterials. While some researchers [40–42] employed

Artificial Neural Networks (ANN) models to predict the vibration and energy absorption characteristics of geofoam, Akis et al. [43] developed ANN models for compressive stresses of geofoam at 1%, 5%, and 10% strains. However, none of the studies included the model dependent evaluation of influencing factors.

In the present study, the effect of density, strain rate, geometry, and ambient temperature on the Modulus of elasticity ( $E_i$ ), compressive stress at 1% Strain ( $\sigma_{1\%}$ ), yield stress ( $\sigma_y$ ), and compressive stress at 10% strain ( $\sigma_{10\%}$ ) of geofoam has been experimentally evaluated by conducting a series of uniaxial unconfined compression tests. In addition, the experimentally evaluated data of this study is also combined with the results from the literature to develop generalised prediction models using ANN and XGBoost algorithms. XGBoost is a latest data-driven advanced ensemble learning-based predictive Machine learning (ML) model [44, 45] that consists of sequential models. The error reported by a preceding model is successively reduced by the following sequential model, resulting in a robust predictive ML model. Statistical checks such as  $R^2$ , mean absolute percent error (MAPE) and root mean square error (RMSE) were incorporated in the study to evaluate the model performances. The study concluded by performing Model Dependent Feature Analysis to assess the factors that influence the compression behaviour of geofoam.

## Materials and methods

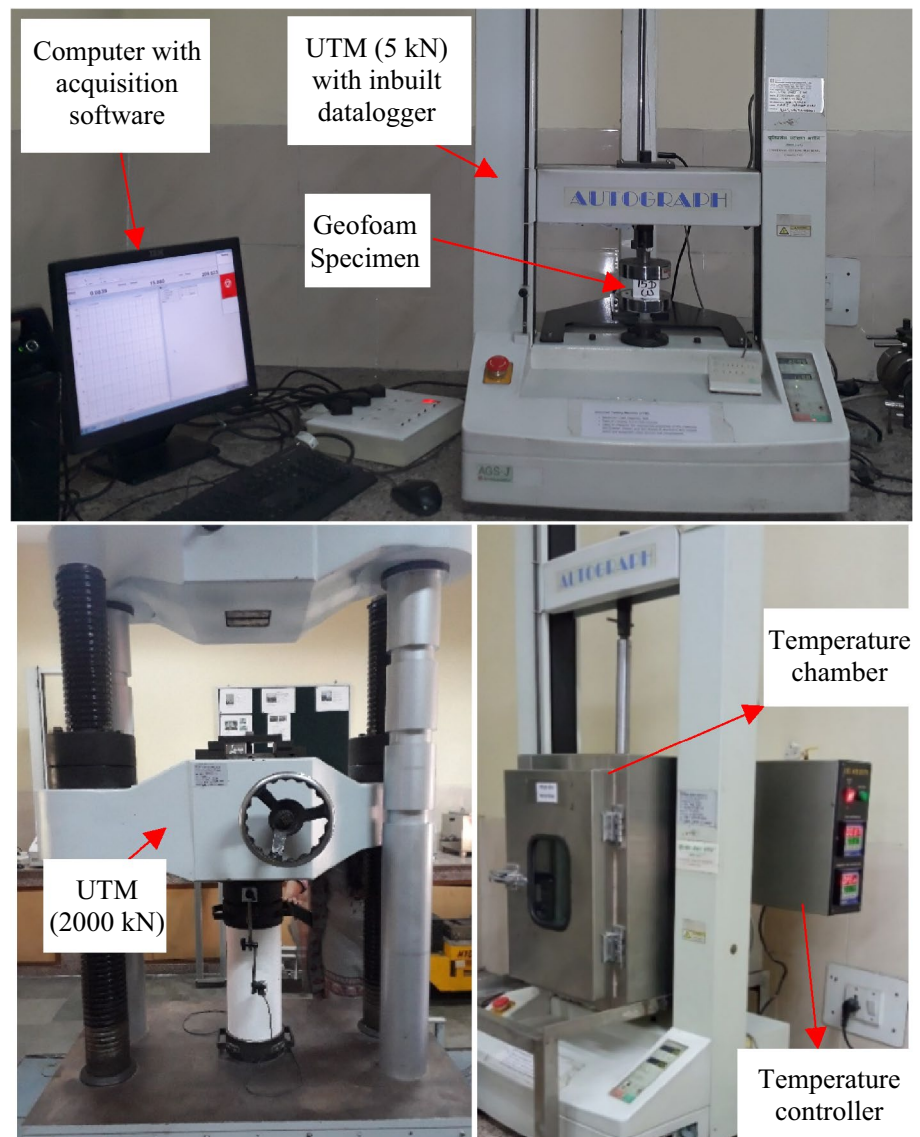
### Materials

EPS geofoam blocks manufactured from three distinct manufacturing units were used in the present study. Geofoam blocks of four different nominal densities, namely 15 kg/m<sup>3</sup>, 20 kg/m<sup>3</sup>, 25 kg/m<sup>3</sup>, and 30 kg/m<sup>3</sup> were collected. These densities are denoted as 15D, 20D, 25D, and 30D, respectively. The specimens of requisite sizes and shapes were cut from the blocks using a hot wire. The apparent density of all cut specimens was determined as per ASTM D1622 [46] to investigate its relevance in compressive behaviour.

### Method

Uniaxial compression tests were performed as per ASTM D1621 [47] on 50 mm specimens in a universal testing machine (UTM) (Model: Shimadzu AGSJ) with a capacity of 5 kN and an accuracy of 0.01 N. Another UTM (Model: Shimadzu UH-2000 kN) with a maximum loading scale range of 20 kN and 0.01 kN accuracy is used for testing larger specimens. The test setup is shown in Fig. 1. The built-in data acquisition system records the load-deformation

**Fig. 1** Compression test set up for elevated temperatures



behaviour seamlessly at 3 ms. Before testing, a seating load of 10–30 N, which corresponds to 0.5% strain, was applied to adjust the alignment of the geofoam. The compressive responses were measured and reported up to 90% strain in the author’s earlier study [48]. However, the present study does not include the compressive responses over 10% strain because it exceeds the serviceability criteria for most geotechnical applications [49].

To assess the influence of strain rate on compression behaviour, tests were also conducted for two different strain rates i.e., 6% and 1%, in addition to the ASTM-prescribed [39] testing strain rate of 10%. The role of temperature on compression behaviour was evaluated by conducting tests at 23 °C, 37 °C and 50 °C. The specimens were kept inside a hot air chamber within the UTM at the testing temperature during and two hours before testing for uniform distribution of temperature throughout the test material. To study the

effect of geometry, specimens of cubical and cylindrical specimens of varying sizes (diameter or width), namely 50 mm, 100 mm and 150 mm, were used. The aspect ratio of the cylindrical specimen was maintained constant at 2. Thus, a total of 122 specimens of varying densities, shapes and sizes subjected to varying loading strain rates and ambient temperatures were assessed. Table 1 summarises the testing strategy adopted for the study.

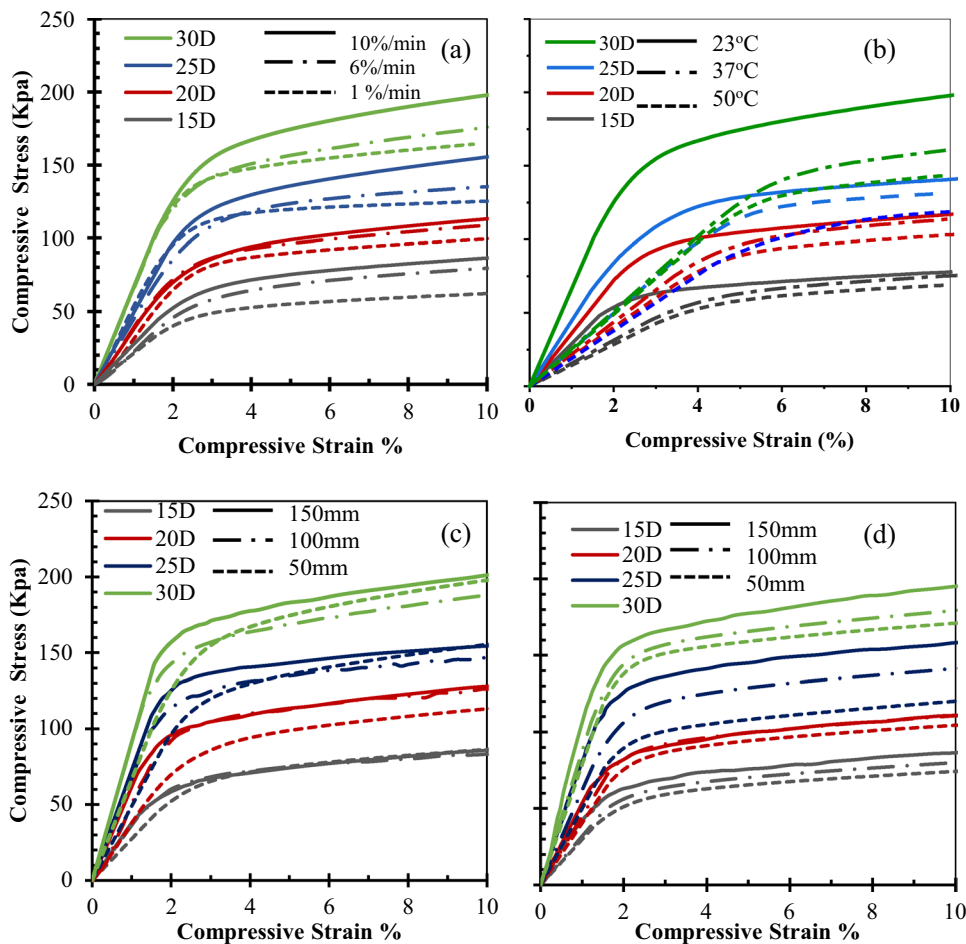
### Test results and analysis

The measured compression responses of various EPS geofoam grades at different testing conditions are shown in Fig. 2. It can be observed that the compressive response of geofoam is linear until 2% strain, followed by yielding, resulting in a plateau region with minimal stress increment

**Table 1** Specimen details and testing conditions

Shape	Size (mm × mm)	Geofoam grade	Strain rate (%/min)	Temperature (°C)
Cube	50 × 50	15D, 20D, 25D, 30D	10, 6, 1	23
Cube	50 × 50	15D, 20D, 25D, 30D	10	23, 37, 50
	50 × 50, 100 × 100, 150 × 150	15D, 20D, 25D, 30D	10	23
Cylinder	50 (∅) × 100 (H), 100 (∅) × 200 (H), 150 (∅) × 300 (H)	15D, 20D, 25D, 30D	10	23

**Fig. 2** Measured compressive behaviour of geofoam under varying **a** strain rate, **b** temperature, **c** cube sizes, **d** cylinder sizes



on increasing strain. Thus, the overall compression behaviour can be classified into three categories: elastic response, yielding and post-yield. For the analysis, stress at three strain levels was considered: Compressive resistance at 1% Strain ( $\sigma_{1\%}$ ), yield stress ( $\sigma_y$ ) and compressive resistance at 10% strain ( $\sigma_{10\%}$ ). The yield point was calculated by employing the double tangent method. The yield strain ranges from 2.3 to 4.7%.

The variation of the stresses and initial modulus with apparent density under varying test conditions is shown in a scatter matrix plot as shown in Fig. 3. The figure shows the importance of different variables considered in the study on the compression parameters. Each plot shows the correlation

between the input ( $\gamma_f$ ) and output parameters ( $\sigma_{1\%}$ ,  $\sigma_y$ ,  $\sigma_{10\%}$  or  $E_i$ ) as well as with each variable (test conditions). The data scatter is quantified using the coefficient of determination (adjusted  $R^2$ ) value of the linear interpolation between the input and output parameters. Adjusted  $R^2$  is used for the evaluation, as it gives a better indication of the accuracy of the linear correlation for multivariable regression problems compared to other coefficient of determination indicators. 95% confidence ellipses, which assume a bivariate normal distribution, are used as visual indicators of correlations between the parameters considered. The confidence ellipse collapses diagonally as the correlation between the input and output parameters approaches 1, whereas they are more

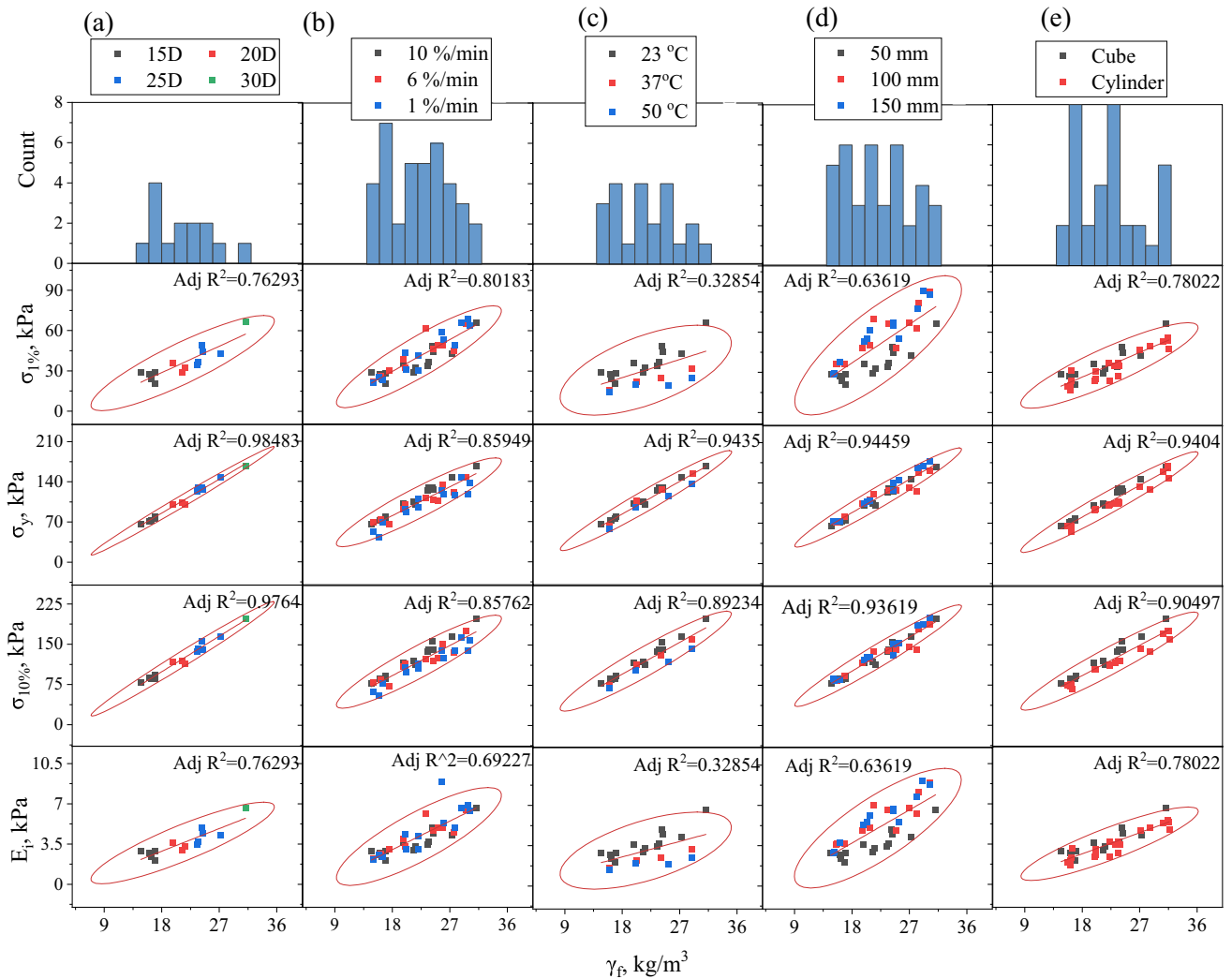


**Fig. 3** Scatter matrices of the test results for varying parameters **a** Nominal density, **b** Strain rate, **c** Temperature, **d** Size, **e** Shape

circular when input and output parameters are uncorrelated. A lower scatter with a high  $R^2$  value and slender ellipses indicates a strong correlation between the input and output parameters and has a negligible influence of other variable conditions considered, such as strain rate, temperature, size, etc. However, a significant influence from the variable parameter on the response is indicated by a higher scatter, low  $R^2$  value, and wide ellipses with systematic shifts in the data points with the variables.

**Effect of density**

As shown in Fig. 2a, the compressive stresses and yield strain increase with an increase in nominal density. The variation of  $E_i$ ,  $\sigma_{1\%}$ ,  $\sigma_y$ , and  $\sigma_{10\%}$  is plotted with respect to apparent and nominal densities in the scatter matrices (Fig. 3a). These stresses and initial modulus significantly depended on and increased with the apparent density. The

observed linear correlations between  $E_i$  and  $\gamma_f$  as well as  $\sigma_{1\%}$  and  $\gamma_f$  indicate only a reasonable convergence (adjusted  $R^2 < 90\%$ ). In contrast, the linear correlations between  $\sigma_y$  and  $\gamma_f$  as well as  $\sigma_{10\%}$  and  $\gamma_f$  indicate excellent convergence (adjusted  $R^2 > 90\%$ ). The confidence ellipse is extremely slender for  $\sigma_y$  and  $\sigma_{10\%}$ . Thus, it can be inferred that the dependency of  $\sigma_y$  and  $\sigma_{10\%}$  on apparent density is more pronounced than that of  $\sigma_{1\%}$  and  $E_i$ . The following empirical correlations relating to compressive resistance and apparent density are derived for standard test conditions prescribed as per ASTM [39] specifications.

$$\sigma_{1\%} = 2.2\gamma_f - 10.7 \tag{1}$$

$$\sigma_y = 6.5\gamma_f - 32 \tag{2}$$

$$\sigma_{10\%} = 7.3\gamma_f - 33.7 \tag{3}$$



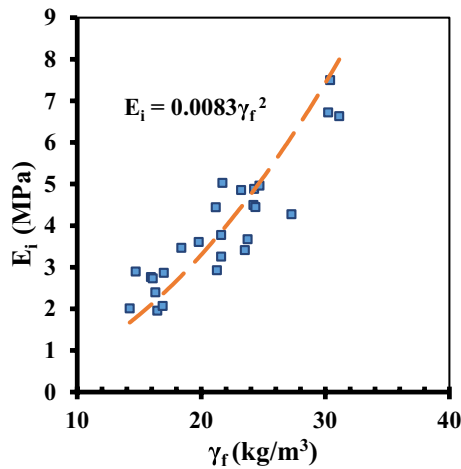


Fig. 4 Variation of modulus of elasticity with apparent density

A theoretical expression correlating the initial modulus ( $E$ ) and density of cellular foams ( $\gamma$ ), derived by Gibson and Ashby [50], is indicated in Eq. 4. On similar lines, an attempt was made here to ascertain the mathematical constant associated with the expression pertaining to EPS geofoam and derive an expression for predicting the initial modulus. Thus, an empirical power expression was developed for the variation of the modulus of elasticity of geofoam ( $E_i$ ) with the apparent density ( $\gamma_f$ ) as shown in Fig. 4. Considering Young's modulus ( $E_p$ ) and density of solid polystyrene polymer ( $\gamma_s$ ) as 2600 MPa and 1050 kg/m<sup>3</sup>, respectively [51], the correlation can be expressed as shown in Eq. 5. Thus, for EPS geofoam having densities ranging from 15 to 30 kg/m<sup>3</sup>, the correlation constant  $C$  can be arrived at as 3.5 for standard testing conditions.

$$\frac{E}{E_p} = C \left( \frac{\gamma}{\gamma_s} \right)^2 \tag{4}$$

$$\frac{E_i}{E_p} = 3.5 \left( \frac{\gamma_f}{\gamma_s} \right)^2 \tag{5}$$

**Effect of strain rate**

It can be observed that the initial response and yield strain are independent of strain rates; however, yield and post-yield compressive stresses increase with an increase in strain rates, as shown in Fig. 2a. This increase in  $\sigma_y$  and  $\sigma_{10\%}$  with strain rate is similar to all geofoam grades and can be attributed to the creep response of the cellular foam. This variation is also indicated by the wide confidence ellipse and low  $R^2$  value in the scatter plot (Fig. 3b).

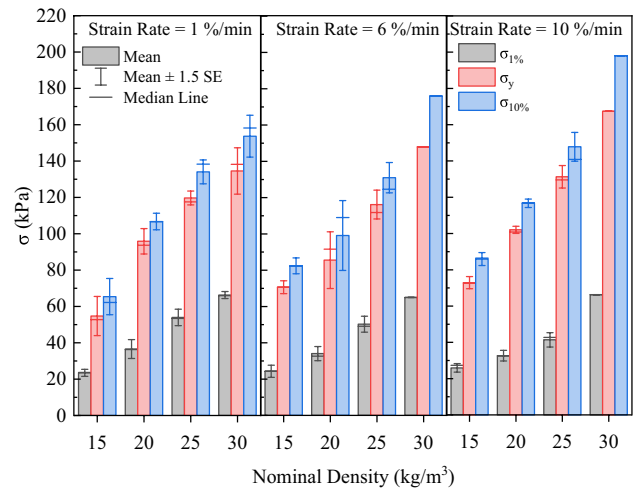


Fig. 5 Variation of compressive stresses with strain rate

The variation of compressive response parameters with strain rate (Fig. 5) indicates an average increase of  $\sigma_{10\%}$  at a rate of 1%, 1.6%, 2% and 2.2% per 1%/min strain rate increment, respectively, for nominal densities 15D, 20D, 25D and 30D. Other researchers have also observed an increase in  $\sigma_{10\%}$  with strain rates in the range of 0.5%–2.2% per 1%/min strain rate increment [31, 43, 52]. Therefore, it is advisable to perform the tests at a strain rate of 1% per minute in order to avoid overestimating the compression parameters. This is in variation with the recommendation of the strain rate in the ASTM specification [39], which specifies a testing strain rate of 10%. It is important to note that the aforementioned specification was primarily formulated for the general use of rigid cellular plastics. However, the present investigation specifically concentrated on load-bearing applications in geotechnical contexts.

**Effect of temperature**

The compressive behaviour in the elastic response range is significantly influenced by temperature, as depicted in Fig. 2b. It has been observed that the yield strain exhibits a twofold increase as the temperature rises from 23 to 37 °C. The variation of the initial compression parameters is also indicated by the very low  $R^2$  value and wide confidence ellipse in the scatter matrix (Fig. 3c).  $\sigma_{1\%}$  and  $E_i$  decrease with the increase in temperature.  $\sigma_y$  and  $\sigma_{10\%}$  also decrease marginally with an increased temperature; however, more pronounced for denser samples.

The variation plots (Fig. 6) demonstrate a decrease in compressive response, as evidenced by a reduction of  $\sigma_{1\%}$  ranging from 40 to 60% with increasing temperature. This corresponds to an average decrease of 3.7% per degree Celsius increment and can be attributed to the thermal-induced

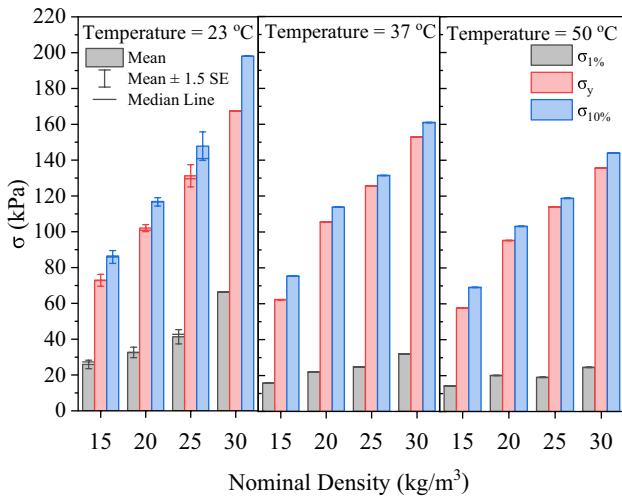


Fig. 6 Variation of compressive stresses with temperature

softening of polystyrene strands. The effect of temperature is more pronounced for denser specimens. Thus, for the 30D specimen, the reduction of  $\sigma_{1\%}$  and  $E_i$  is higher than in the 15D specimen. The reduction in the  $\sigma_{10\%}$  value for the 15D, 20D, 25D, and 30D specimens were determined to be 0.34 kPa, 0.53 kPa, 0.84 kPa, and 2.0 kPa per degree Celsius, respectively. Zou and Leo [38] reported the corresponding value as 0.46 kPa per degree Celsius for the 20D specimen.

**Effect of size**

Figure 2c and d show the stress–strain curves of geofoam under varying sizes for cubical and cylindrical specimens, respectively. It can be inferred that the size significantly impacts the initial elastic response of geofoam. This is also indicated by the low  $R^2$  value of the scatter plot (Fig. 3d). In the case of cube-shaped specimens, negligible effect of size is observed for  $\sigma_y$  and  $\sigma_{10\%}$ . However, for cylindrical specimens, due to an increase in bead population, a marginal increase in  $\sigma_y$  and  $\sigma_{10\%}$  with size is observed, as shown in

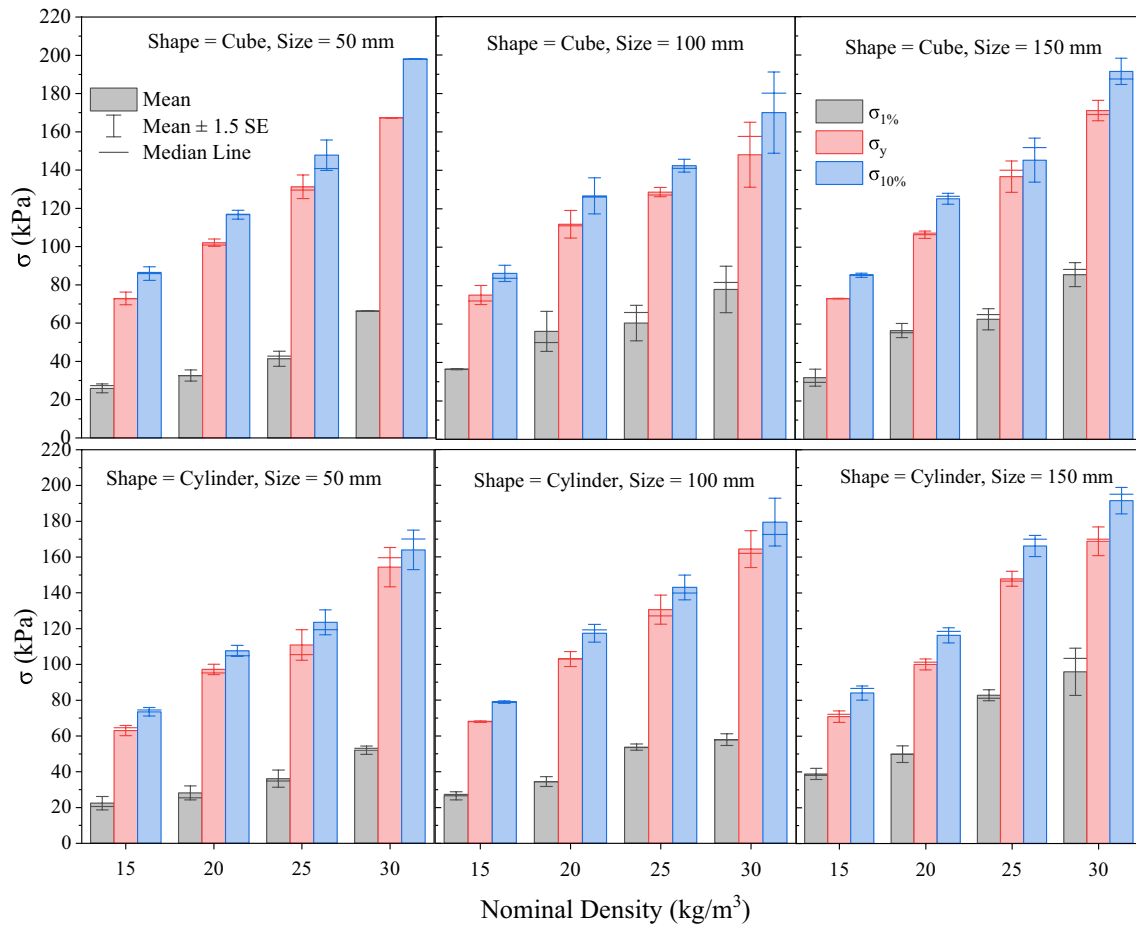


Fig. 7 The variation of compressive stresses with block size and shape

Fig. 7.  $E_i$  increases by 60% when size increases from 50 to 100 mm, after which negligible increment is observed. This is in consistent with the observations reported by Atmatzidis et al. [26]. Elragi et al. [30] further observed an  $E_i$  value increment of 100% when the size increases from 50 to 600 mm.

### Effect of geometry

From Fig. 7, it can be inferred that shape does not have significant influence on the initial elastic response of geofoam. The  $\sigma_{1\%}$ ,  $\sigma_y$  and  $\sigma_{10\%}$  of cubical specimens are slightly higher than cylindrical specimens of the same size for all the geofoam grades. This can be attributed to the increased bead quantity for cubical specimens relative to the cylindrical specimens, having diameter same as the cube size. However, the high value of  $R^2$  in the scatter plot (Fig. 3e) indicates a relatively uniform distribution. Consequently, it is reasonable to infer that both shapes exhibit comparable responses. Testing on cubical samples is recommended because of the ease of moulding and cutting.

### Data analysis and identification of influencing factors

The data analysis of the laboratory test results on geofoam is conducted to analyse the input and output data quality. The statistical description of the experiments conducted in the laboratory is elucidated in Table 2. The count refers to the number of specimens available, and the mean is the representative central tendency of the data, Std. Dev. expresses the deviation from the mean; the variance is the spread between numbers in a feature in a data set which assesses the dispersion of data points around the mean; min is the minimum value of the feature in the dataset; max refers to its maximum value followed by varying percentile values of

each feature. Since the shape is a categorical parameter, this study indicates its influence through aspect ratio. It is worth noting that, with the exception of apparent density, all other independent variables are interval data points. The skewed distribution of these independent variables is evident from the quartiles. The high variance in the dependent variables, specifically the compressive stresses, emphasises the strong necessity for the development of prediction models.

In addition to statistical analysis of the experimental data, correlation coefficients were developed to observe the interdependency of the input and output parameters considered in the study. Given that the majority of the independent variables are of the interval data type, it can be argued that rank correlation provides a more accurate measure of the interdependence between these variables as compared to Pearson's correlation. Therefore, Spearman's rank correlation coefficient ( $r_s$ ) is employed for assessing the correlation between two parameters and is calculated using the following formula [53].

$$r_s(X_i - Y_i) = 1 - \frac{6 \sum_{i=1}^n (X'_i - Y'_i)^2}{n(n^2 - 1)} \quad (6)$$

where  $X'_i$  and  $Y'_i$  are the ranks of  $X_i$  and  $Y_i$ , respectively, and  $n$  is the number of datasets. The Spearman's rank correlation coefficient for all the input and output parameters is shown as a heat map in Fig. 8. A positive coefficient indicates direct proportionality, whereas a negative coefficient indicates inverse proportionality. The perfect correlation is indicated by a correlation coefficient of 1.0. The significance of the correlation coefficient, explained by Chan [54], is shown in Table 3.

It can be said that the apparent density of geofoam is the most positive influential parameter for the compressive resistance of geofoam. The effect of density on  $\sigma_y$  and  $\sigma_{10\%}$  is the strongest, whereas it is moderate on  $\sigma_{1\%}$  and  $E_i$ . The second most important parameter, which plays a significant

**Table 2** Statistical analysis of input data from the experimental study

	Independent variables					Dependent variables			
	Apparent Density (kg/m <sup>3</sup> )	Temperature (°C)	Size (mm)	Aspect ratio	Strain rate (%/min)	$\sigma_{1\%}$ (kPa)	$\sigma_{10\%}$ (kPa)	$\sigma_y$ (kPa)	$E_i$ (MPa)
Count	122	122	122	122	122	122	122	122	122
Mean	22.455	24.344	82.787	1.426	8.68	44.902	124.959	111.074	4.513
Std. Dev	5.157	5.363	39.507	0.497	2.898	19.718	36.396	34.094	2.015
Variance	26.591	28.757	1560.76	0.247	8.401	388.80	1324.70	1162.43	4.059
Min	14.720	23	50	1	1	14.000	56.000	43.000	1.430
Max	32.980	50	150	2	10	106.00	214.00	190.00	10.59
25%	17.130	23	50	1	10	29.000	92.250	79.750	2.907
50%	22.300	23	50	1	10	42.50	120.50	107.00	4.220
75%	27.175	23	100	2	10	55.75	150.00	134.50	5.585



**Fig. 8** Heat map of correlation coefficients

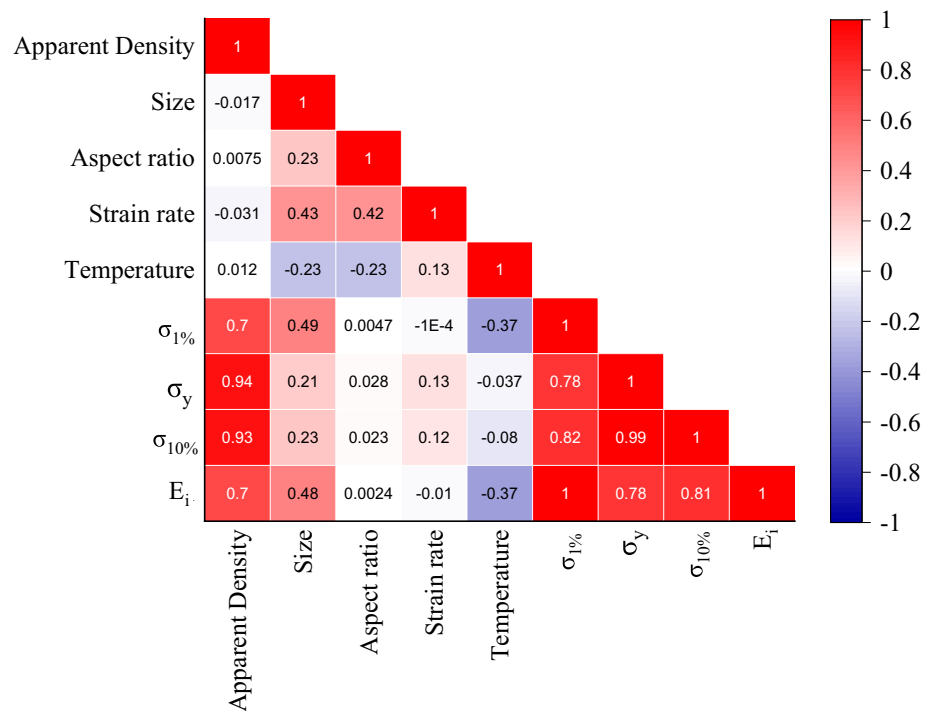


**Table 3** Interpretation of Spearman’s rank correlation coefficient

$ r_s $	Correlation	Parameters
0–0.10	None	$\sigma_{1\%}$ , $\sigma_y$ , $\sigma_{10\%}$ , E versus aspect ratio $\sigma_{1\%}$ , E versus strain rate $\sigma_y$ , $\sigma_{10\%}$ versus temperature
0.10–0.29	Poor	$\sigma_y$ , $\sigma_{10\%}$ versus size $\sigma_y$ , $\sigma_{10\%}$ versus strain rate
0.30–0.59	Fair	$\sigma_{1\%}$ , E versus temperature $\sigma_{1\%}$ , E versus size
0.6–0.79	Moderate	$\sigma_{1\%}$ , E versus apparent density
0.8–0.99	Very strong	$\sigma_y$ , $\sigma_{10\%}$ versus apparent density

role in the compressive behaviour, is size. The initial compressive behaviour is found to be fairly affected by the specimen size. Temperature negatively influences the initial compressive behaviour, whereas the strain rate positively influences the compressive behaviour after yielding. Based on the results of the correlation analysis, it can be inferred that there is no significant impact of the shape and aspect ratio on the compressive behaviour.

### ML predictive models

Based on the test results, ML models were developed for the prediction of  $\sigma_{1\%}$ ,  $\sigma_{10\%}$ , and  $\sigma_y$  with independent input parameters of uniaxial compression tests. Data-driven models based on ANN and XGBoost were developed and checked for accuracy. ANN is one of the basic prediction

model widely used for the compressive strength of different materials in the past two decades [43, 55–57]. Neural networks are highly flexible and powerful in modeling non-linear relationships and complex patterns in the data. Thus, in the present problem statement, where the relationships between different input features are not pre-determined and well-defined, ANN has been used by the authors. Furthermore, the study chose the XGBOOST algorithm because it stood out as one of the most refined among boosting machine learning (BML) algorithms, driven by its superior performance documented in literature for characterizing the compressive strength of diverse geomaterials [58–61]. XGBoost algorithm is based on boosting technique and is an implementation of gradient-boosted trees that is most effective in handling a variety of data types, distributions, and relationships through an ensemble of decision trees and continuous reduction of errors. Since the features in the problem statement have non-linear relationships, the authors have also used XGBoost for the development of the model in the present study. Eight key processes are involved in the development of the optimised model, and each stage is described in detail as follows:

- i. *Database preparation:* Initial database was prepared from the experimental study.
- ii. *Preliminary data evaluation:* Preliminary data analysis was conducted using statistical evaluation. Correlation analysis for the interdependency of various parameters was also assessed.

- iii. *Data matrix expansion*: More data was collected from relevant literature and compiled appropriately.
- iv. *Data pre-processing*: Data was analysed using statistical evaluation, and missing values were identified to arrange the acquired data. It was followed by normalising the dataset in preparation for model building.
- v. *Model selection*: ANN and XGBoost were utilised for the prediction and evaluation of the models.
- vi. *Hyperparameter optimisation*: Hyperparameters that lead to the development of the most accurate and generalised ML models were selected.
- vii. *Model evaluation*: All models were compared, and the best-performing algorithms were selected based on evaluation metrics, i.e.,  $R^2$ , RMSE, MAE, MSE, and MAPE.
- viii. *Analysis and reporting*: The findings were reported by comparing various models considered, optimisation parameters, and evaluation metrics.

## Data compilation

To facilitate the development of a comprehensive model, it is imperative to acquire a large dataset wherein ML models can be trained and tested. A commonly used rule of thumb for dataset sample size requirements for neural networks is that the sample size should be at least 10 to 20 times the number of trainable parameters in the model [62, 63]. Some researchers suggested that, for real-world problems, the minimum data size requirement should be increased to 30 times the number of trainable parameters as a precautionary measure [64]. This guideline helps ensure that the model has sufficient data to learn meaningful patterns without overfitting to the training data. Consequently, the findings documented in existing literature pertaining to the uniaxial compressive strength test conducted on geofoam were collected and integrated with the test results presented by the

authors of this study. This assertion is supported by the evidence that the manufacturing process has a minimal impact on the mechanical characteristics of EPS blocks [65]. The stress–strain characteristics of geofoam have been extensively investigated with respect to apparent density, size, aspect ratio, and strain rate. However, the influence of temperature on these properties is yet to be fully investigated. Until now, no prior research has investigated such a large number of test variables as the present study, with a specific focus on incorporating temperature as a variable. Therefore, to achieve a larger dataset for developing models, the influence of temperature observed in the experimental datasets was excluded. A database of 555 test results was compiled, which comprised the test results conducted by the authors and the results reported in the literature [24–26, 43, 66–68]. A subset of these studies did not include data on yield stress. These can be considered as missing value. In such cases,  $\sigma_y$  is estimated by dividing  $\sigma_{10\%}$  using a reduction factor of 1.3 [40]. Therefore, the imputation technique employed in the present study involves replacing missing values with information derived from previous domain knowledge. In general,  $E_i$  is estimated to be 100 times  $\sigma_{1\%}$ ; thus, it is not considered in the ML models. The statistics of the expanded dataset are presented in Table 4. It may also be noted that the prediction models are valid only for range of input parameter data considered in the table.

## Development of ML models

In this study, ML models, based on ANN and XGBoost algorithms, were developed to predict the values of  $\sigma_{1\%}$ ,  $\sigma_{10\%}$ , and  $\sigma_y$  on Python 3.10. The dataset comprising 555 test results was randomly divided into training and test datasets in a 70:30 ratio. The models were developed on 70% of the data, the accuracy of which was tested on the remaining 30% of the dataset.

**Table 4** Statistical description of the expanded database

	Independent variables				Dependent variables		
	Apparent density (kg/m <sup>3</sup> )	Size (mm)	Aspect ratio	Strain rate (%/min)	$\sigma_{1\%}$ (kPa)	$\sigma_{10\%}$ (kPa)	$\sigma_y$ (kPa)
Count	555	555	555	555	555	555	555
Mean	21.631	80.874	1.003	96.050	45.668	109.256	135.234
Std. Dev	5.721	42.005	0.420	197.200	20.983	41.671	49.440
Variance	32.734	1764.443	0.176	38,887.907	440.294	1736.487	2444.266
Min	9.980	50	0.38	0.5	5	22	31
Max	44.790	300	2	2000	125	329	351
25%	15.375	50	1	10	28	68	86
50%	22.240	65	1	10	45	110	137
75%	26.000	100	1	100	57	141	176

Statistical metrics were used to test the accuracy of the models in terms of coefficient of determination ( $R^2$ ), mean square error (MSE), root mean square error (RMSE), mean absolute error (MAE) and mean absolute percent error (MAPE). The mathematical formulations of these parameters are defined in Eqs. 3–7.

$$R^2 = 1 - \frac{\sum_{i=1}^n (y_i - y'_i)^2}{\sum_{i=1}^n (y_i - \bar{y})^2} \tag{7}$$

$$MSE = \frac{1}{n} \sum_{i=1}^n |y_i - y'_i|^2 \tag{8}$$

$$RMSE = \sqrt{\frac{1}{n} \sum_{i=1}^n |y_i - y'_i|^2} \tag{9}$$

$$MAE = \frac{1}{n} \sum_{i=1}^n |y_i - y'_i| \tag{10}$$

$$MAPE = \frac{1}{n} \sum_{i=1}^n \left| \frac{y_i - y'_i}{y_i} \right| \tag{11}$$

where  $y'$  and  $y$  are the predicted and measured values, respectively, while  $n$  is the total number of test datasets and  $\bar{y}$  is the mean of measured values.  $R^2$  assesses how well the model reproduces the observed outputs. The values of  $R^2$  range from 0 to 1, with higher fitting optimisation reported if the value is closer to 1. The values MSE, MAE, MAPE, and RMSE are used to evaluate modelling error, wherein the smaller the value, the lesser the difference between the predicted and measured values.

**ANN**

ANN is a highly parallel distributed processor that has a natural propensity for storing experiential knowledge and making it available for use [69]. It is widely used to predict output from a dataset comprising independent variables. The neural network of the ANN model consists of several neurons stacked in layers, which act as the primary processing element of the neural network. Data is received, weighed, processed, and subsequently transferred from neurons of one layer to the next.

In this study, three independent ANN models were developed to predict the values of  $\sigma_{1\%}$ ,  $\sigma_{10\%}$ , and  $\sigma_y$  based on the independent input parameters of uniaxial compression tests. Each model was trained on the same input parameters, namely the size and aspect ratio of the geofoam specimen,

the density of the material, and the strain rate at which the uniaxial compression test was performed.

A hidden layer often results in giving reasonable accuracy [70]. In the current study, as the dataset is not very large but can be considered a medium-sized dataset, a simple network architecture comprising only a single hidden layer with 6 neurons has been considered to avoid overfitting. According to Erzin et al. [71], the maximum number of neurons in the hidden layer cannot be greater than  $2i + 1$ , where  $i$  is the number of input parameters. Since the number of input parameters for each model is 4, the limiting number of neurons in the hidden layer for the models has been restricted to 9. To achieve an optimum number of neurons in the hidden layer, one neuron was fitted in the hidden layer for each model and was gradually increased to the upper limit. Based on the comparison of the measured and predicted values during the trials, six neurons in the hidden layer of each ANN model were used in this study, the structure of which is illustrated in Fig. 9. Thus, the total number of trainable parameters for this feed-forward neural network is 30. In this study, the ratio of data size to the number of trainable parameters or weights stands at 18, which is deemed adequate considering similar models for material strength predictions [43, 72–74]. The combination of exponential linear unit (ELU) and rectified linear unit (ReLU) has been used as the activation function for the neural layers. Activation functions convert the weighted input received at a neuron of a layer to an output, which is then used as input by the subsequent layer.

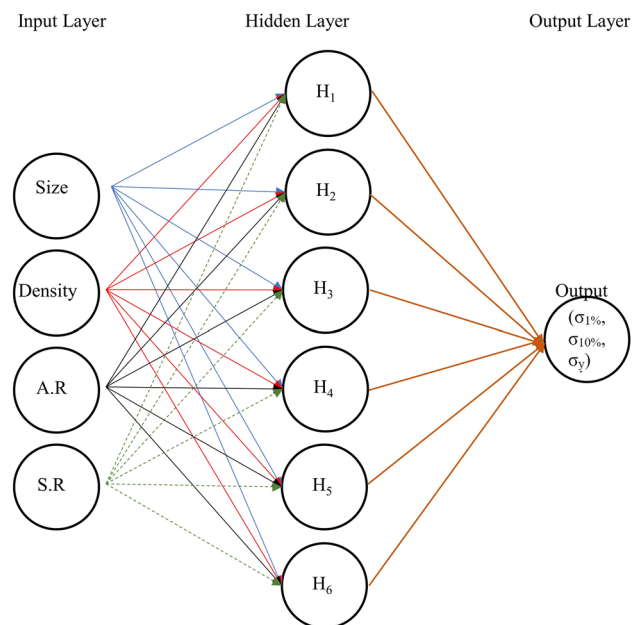


**Fig. 9** Architecture of the ANN model

## XGBOOST

XGBoost is an ensemble learning algorithm developed by Chen and Guestrin [75] and belongs to the boosting family. A model based on the boosting principle produces sequential models to solve the same problem such that each sequential model focuses on the training data values that the previous model inaccurately predicted. The models developed in each sequence are known as weak learners, which, when combined, develop a strong learner. The weak learner is usually defined as a decision tree, which is a supervised ML technique. The tree structure consists of internal nodes, branches, and leaves [76]. Internal nodes correspond to the dataset's features, branches represent the decision rules, and leaves signify the output variables. The algorithm of XGBoost improves the traditional boosting algorithms to minimise overfitting and provide better predictions. The gradient boosting algorithm consists of a loss function to be optimised, a weak learner to make predictions and an additive model to add weak learners to minimise the loss function. XGBoost model, through an iterative procedure, optimises the objective function by updating parameters in a sequential step using residuals from the previous step. The most significant benefit of XGBoost is its scalability across any condition [77]. In general, the XGBoost algorithms are the evolution of decision tree algorithms that were improved over time.

Three XGBoost models were developed for the prediction of  $\sigma_{1\%}$ ,  $\sigma_{10\%}$ , and  $\sigma_y$  values. The hyperparameter tuning of the models was performed using fivefold cross-validation, and the values were optimised using the “*Random-SearchCV*” function in Scikit-learn 0.24.2 [78].

## Results and discussion

A comparison of the predicted values of  $\sigma_{1\%}$ ,  $\sigma_{10\%}$ , and  $\sigma_y$  obtained from ANN and XGBoost models used in this study is made against the values obtained through laboratory experiments for both training and testing datasets and is illustrated in Fig. 10. Higher the alignment of the values against the diagonal, the better the ML model's performance. It can be observed that the performance of both ANN and XGBoost models is reasonable as well as comparable. On comparing the models, it can also be observed that for the training dataset of the XGBoost model, the points are near the ideal, i.e.,  $y=x$  line, indicating that the predicted values are close to the experimental results and thereby result in a high  $R^2$  value. For the ANN model, a relatively higher data scatter can be observed away from the diagonal, indicating a significant difference between true and predicted output values by the corresponding model. For the testing data, the XGBoost model presents higher accuracy than ANN, as it can be seen that the scattering of points is more widely

spread than XGBoost, which results in lower RMSE and MAPE values for the XGBoost model. The predicted results of the testing dataset that disperse away from the diagonal indicate less accuracy in the prediction of a testing dataset. It is thus evident that the XGBoost model predicts the values of  $\sigma_{1\%}$ ,  $\sigma_{10\%}$ , and  $\sigma_y$  with high accuracy, robustness, and generalisation. While the models perform accurately for both training and testing datasets to predict  $\sigma_y$  values, the performance is relatively inaccurate for the prediction of  $\sigma_{1\%}$  as observed from the statistical metrics of the models summarised in Table 5.

The  $R^2$  value for each model is greater than 0.8 for both the training and testing dataset. This indicates that the predictions obtained from the models are significantly correct. As expected, the accuracy of all the testing dataset is equal to or lower than that of the training dataset, except for the ANN and XGBOOST models of  $\sigma_{1\%}$ . However, the  $R^2$  value, which assesses a regression problem better, is lower for the testing dataset compared to the training dataset for all the models. Relative to the average values of  $\sigma_{1\%}$ ,  $\sigma_{10\%}$ , and  $\sigma_y$ , the RMSE value lies within 5–20% of the actual values, with a higher error being observed in the prediction of  $\sigma_{1\%}$ . The low  $R^2$  value achieved for testing the  $\sigma_{1\%}$  using ANN and XGBOOST indicates that the issue is primarily due to the variability in the data rather than a modelling error. This suggests that to enhance the reliability of the developed model in predicting values of  $\sigma_{1\%}$  improved data incorporating additional input parameters is required, which stands as a limitation of the current study. The omission of the input parameter temperature in the development of ML models is another clear limitation of the current study. Additionally, the developed models are incapable to predict the long-term compressive strength of geofoam. Further experimental data is necessary to anticipate the compressive behaviour of geofoam under sustained loading conditions and to predict its creep effects.

## Visualization of errors

To visualise the error in the predictions of  $\sigma_{1\%}$ ,  $\sigma_{10\%}$ , and  $\sigma_y$  with respect to true values, residual error plots were plotted. Figure 11 shows the residual error plots of the models. The residual error is the measure of the dispersion of a point vertically from the regression line. It measures the error between the predicted and true values of the target. The higher the residual dispersion from the origin ( $y=0$  lines), the lower the accuracy of the model. The residual plot of the XGBoost model has the highest density of points close to the origin with a minimum dispersion of points away from the origin. On the other hand, the residual plots of the ANN models demonstrate high density away from the origin and low density close to the origin. No model can exhibit null

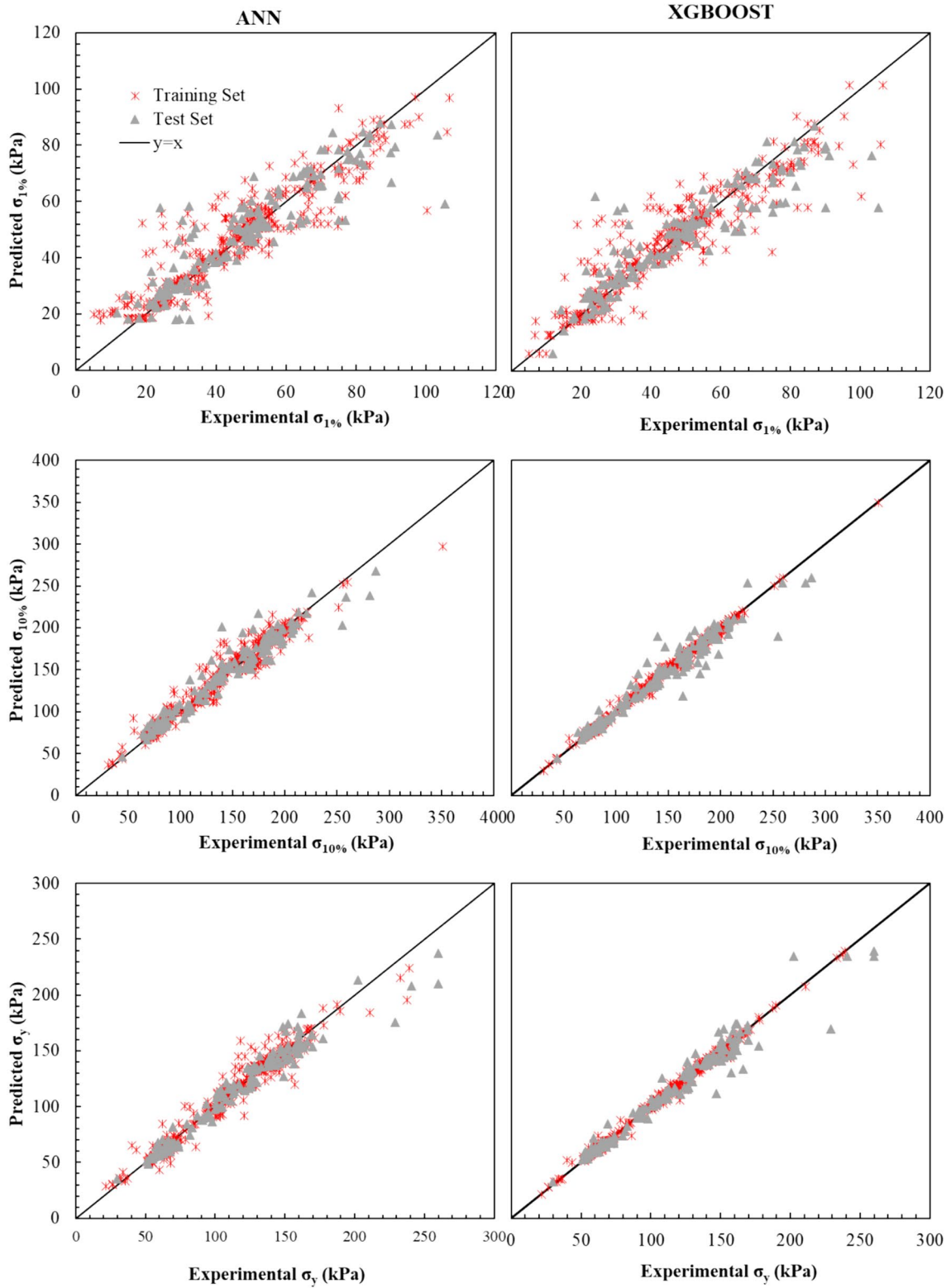


**Fig. 10** Plot between the observed and the predicted values for training and testing datasets for  $\sigma_{1\%}$ ,  $\sigma_{10\%}$ , and  $\sigma_y$



**Table 5** Summary of comparison between various prediction models

Parameter	Model	Statistical indices					
		R <sup>2</sup>	MSE	RMSE	MAPE	MAE	Accuracy
$\sigma_{1\%}$	ANN_train	0.85	63.32	7.96	16.19	5.37	83.81
	ANN_test	0.83	78.65	8.87	14.03	5.80	85.97
	XGBoost_train	0.85	59.84	7.73	13.54	5.06	86.4
	XGBoost_test	0.80	91.64	9.57	12.9	5.79	87.08
$\sigma_{10\%}$	ANN_train	0.95	117.75	10.85	6.04	7.55	93.96
	ANN_test	0.94	153.93	12.41	6.01	8.22	93.99
	XGBoost_train	0.99	13.46	3.67	1.92	2.37	98.08
	XGBoost_test	0.95	135.73	11.65	4.66	6.86	95.34
$\sigma_y$	ANN_train	0.95	81.51	9.03	5.64	5.77	94.36
	ANN_test	0.95	91.67	9.57	5.34	6.29	94.66
	XGBoost_train	0.99	7.9	2.81	1.9	1.79	98.1
	XGBoost_test	0.95	83.73	9.15	4.15	5.08	95.85

residual errors; however, a good model, such as XGBoost, exhibits only minor random errors.

### Relative importance of influencing factors

The ‘feature importance’ of different parameters is evaluated using the XGBoost model, which determines the degree of usefulness of a specific input parameter for the model and prediction. XGBoost model was selected for this analysis, as it outperformed the ANN model. This gives an insight into the relative importance of the influence factors on the compressive response at different strains considered in the study. In this analysis, the variations of each input parameter are analysed by eliminating a single parameter from the dataset exclusively while keeping the remaining input parameters unchanged. The XGBoost model is then run on these datasets after randomly shuffling the values of a selected input while keeping the remaining input unchanged to predict the new output. The relative importance of each input parameter is determined by comparing the RMSE associated with it to that of other parameters. Other researchers used a similar approach for predicting the relative importance of variables on the performance of various geomaterials [44, 79, 80]. It may be noted that this analysis is a model-dependent feature importance study, whereas Spearman’s correlation developed earlier is a model-agnostic feature importance study. This analysis considers the contribution of all the input variables in a combined form to predict the output. In contrast, the heat map developed using Spearman’s correlation only considers the correlation between two parameters. This also considers a generalised model of a wider data range in contrast to Spearman’s correlation developed for the results of the experimental study conducted by the authors.

The relative importance of the parameters considered in this study for the compressive response prediction is indicated in Fig. 12. Apparent density is the most significant influencing factor for all the stress levels. However, its relative importance is more for  $\sigma_{10\%}$ , and  $\sigma_y$ . The XGBoost model also indicates significant importance in aspect ratio followed by size on  $\sigma_{1\%}$  output. However, its effect diminishes during yield and post-yielding. It may also be noted that the specimen’s height has a greater impact on the value of  $\sigma_{1\%}$  than the specimen’s width (expressed as size). Strain rate has only a minor influence on the compressive responses of geofoam.

### Conclusions

In the present study, the effect of density, temperature, strain rate, and geometry on the compressive behaviour of EPS geofoam was characterised using a series of uniaxial compression tests. Machine learning models based on ANN and XGBoost were then developed to predict the values of  $\sigma_{1\%}$ ,  $\sigma_y$ , and  $\sigma_{10\%}$  using four input parameters, namely size of the geofoam, apparent density of the material, aspect ratio of the specimen, and the strain rate of testing. As the size of database is critical for developing a robust predictive model, 433 tests results from the literature were compiled, making a database of 555 number of tests that included the experiments conducted by the authors in this study. Following are the salient observations made from the study:

- The apparent density was the most important parameter influencing the compressive behaviour of geofoam. The influence of apparent density was more pronounced post-yield than the initial elastic response. However, the influ-

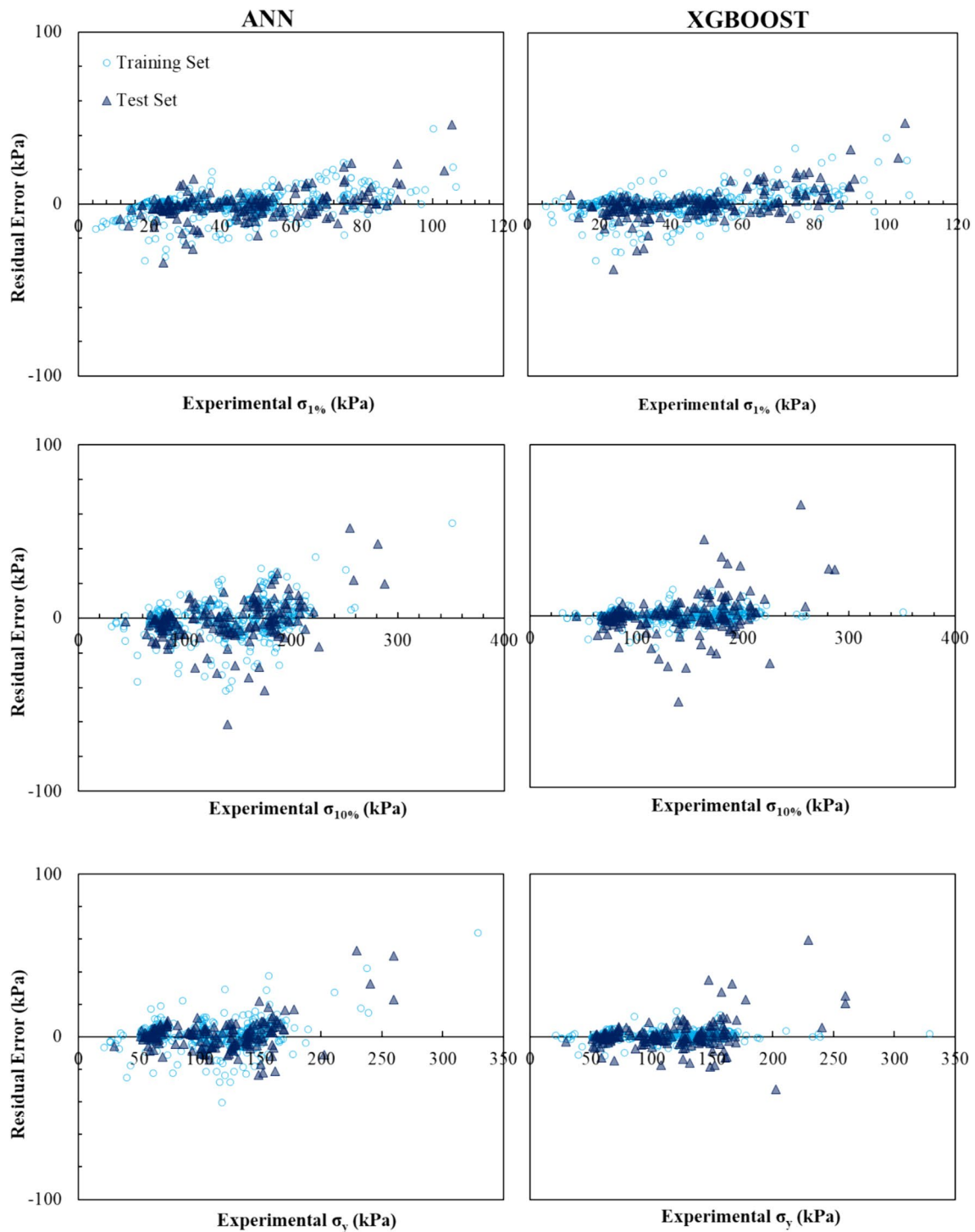
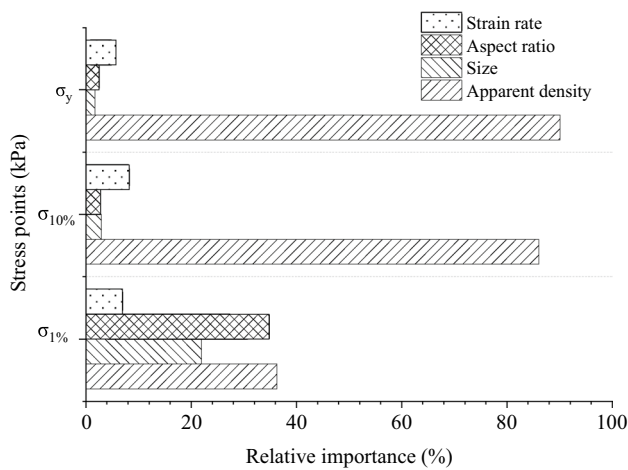


Fig. 11 Residual Plots for ANN and XGBOOST

- The elastic response of geofom was found to be significantly influenced by the ambient temperature. It was observed that the modulus of elasticity of geofom decreased by 3.7% for every one-degree Celsius increase in temperature. The yield strain doubled as the temperature increased from 23 to 37 °C. Therefore, it
- An increase in testing strain rate marginally increases the post-yield stresses. A strain rate of 1%/min is recommended for the quality testing of geofom for geotechnical applications.



**Fig. 12** Relative importance of different input variables

is advisable to conduct testing at the highest ambient temperature of the proposed site in addition to the conventional temperature conditions.

- The size of the specimen demonstrated a positive influence on the initial elastic response of geofoam. The modulus of elasticity increased by 1.6 times when the size was increased from 50 to 100 mm, after which a negligible increment was seen. The geometry and aspect ratio were found to have an insignificant influence on compressive behaviour.
- Developed prediction models using ANN and XGBoost, provide reasonable and reliable results for the geofoam compression parameters. XGBoost outperforms ANN in predicting the compressive behaviour parameters with MAPE values of 12.2, 4.15 and 4.66 respectively for  $\sigma_{1\%}$ ,  $\sigma_{\gamma}$ , and  $\sigma_{10\%}$ . The  $R^2$  values for each model in both the training and testing dataset were greater than 0.8, with an accuracy higher than 80% in each case. The success of the developed models is underscored by the respective overall accuracies achieved for the XGBoost models, which were 88%, 96% and 95% for  $\sigma_{1\%}$ ,  $\sigma_{\gamma}$ , and  $\sigma_{10\%}$ .
- The feature importance analysis using the XGBoost model revealed that density is a significant parameter influencing stresses at all strain levels with relative importances of 36%, 90% and 86% respectively for  $\sigma_{1\%}$ ,  $\sigma_{\gamma}$ , and  $\sigma_{10\%}$ . Additionally, the size and aspect ratio of the geofoam also have an impact on the initial response of its compression behaviour with relative importances of 22% and 35% respectively. Test strain rate also has an influence on the overall compressive response. The result of this study depicts that systematically trained ML models can be easily utilised to comprehend the compressive behaviour of geofoams by employing the experimental data parameters.

- The constraints of the present study encompass inadequate supplementary experimental data required for developing models to predict the behaviour across broader temperature ranges, along with the absence of creep effects consideration in the developed models' analysis of the compressive response of geofoam.

**Supplementary Information** The online version contains supplementary material available at <https://doi.org/10.1007/s41062-024-01606-2>.

**Acknowledgements** This work was supported by the National Highways and Infrastructure Development Corporation Limited, New Delhi, India, under Grant [GAP-4658] to Council of Scientific and Industrial Research—Central Road Research Institute (CSIR—CRRI), New Delhi, India 110025. The approval of the Director, CSIR—CRRI, to publish this research paper is also acknowledged.

**Author contributions** Conceptualization: Parvathi Geetha Sreekantan; Methodology: Parvathi Geetha Sreekantan; Aali Pant; G. V. Ramana; Investigation: Parvathi Geetha Sreekantan Analysis: Parvathi Geetha Sreekantan; Aali Pant Funding acquisition: Parvathi Geetha Sreekantan Writing—original draft: Parvathi Geetha Sreekantan; Aali Pant; Writing—review and editing: G. V. Ramana; Supervision: G. V. Ramana.

**Funding** National Highways & Infrastructure Development Corporation Limited, New Delhi, India, GAP-4658, Parvathi Geetha Sreekantan.

**Data availability** The datasets generated during and analysed during the current study are available as supplementary data files.

## Declarations

**Conflict of interest** On behalf of all authors, the corresponding author states that there is no conflict of interest.

**Ethical approval** Not applicable.

**Consent to participate** All authors agreed to participate in this study.

**Consent for publication** All authors agree to publish.

## References

1. Bartlett SF, Amini Z (2019) Design and evaluation of seismic stability of free-standing EPS embankment for transportation systems. In: Arellano D, Özer AT, Bartlett SF, Vaslestad J (eds) 5th international conference on geofoam blocks in construction applications. Springer International Publishing, Cham, pp 319–330
2. Farnsworth CB, Bartlett SF, Negussey D, Stuedlein AW (2008) Rapid construction and settlement behavior of embankment systems on soft foundation soils. *J Geotech Geoenviron Eng* 134:289–301. [https://doi.org/10.1061/\(ASCE\)1090-0241\(2008\)134:3\(289\)](https://doi.org/10.1061/(ASCE)1090-0241(2008)134:3(289))
3. Zou Y, Small JC, Leo CJ (2000) Behavior of EPS geofoam as flexible pavement subgrade material in model tests. *Geosynth Int* 7:1–22. <https://doi.org/10.1680/gein.7.0163>

4. Puppala AJ, Ruttanapomakul P, Congress SSC (2019) Design and construction of lightweight EPS geofoam embedded geotext embankment system for control of settlements. *Geotext Geomembr* 47:295–305. <https://doi.org/10.1016/j.geotextmem.2019.01.015>
5. Saride S, Puppala AJ, Williammee R, Sirigiripet SK (2010) Use of lightweight ECS as a fill material to control approach embankment settlements. *J Mater Civ Eng* 22:607–617. [https://doi.org/10.1061/\(ASCE\)MT.1943-5533.0000060](https://doi.org/10.1061/(ASCE)MT.1943-5533.0000060)
6. Burugupelly NK, Dasaka SM (2022) Effect of EPS geofoam on lateral earth pressure reduction a numerical study. In: Satyanarayana Reddy CNV, Krishna AM, Satyam N (eds) *Dynamics of soil and modelling of geotechnical problems*. Springer Singapore, Singapore, pp 231–241
7. Lakkimsetti B, Latha GM (2023) Effectiveness of different reinforcement alternatives for mitigating liquefaction in sands. *Int J Geosynth Ground Eng* 9:37. <https://doi.org/10.1007/s40891-023-00459-6>
8. Meguid MA, Ahmed MR, Hussein MG, Omeman Z (2017) Earth pressure distribution on a rigid box covered with U-shaped geofoam wrap. *Int J Geosynth Ground Eng* 3:1–14. <https://doi.org/10.1007/s40891-017-0088-4>
9. Khan MI, Meguid MA (2021) A numerical study on the role of eps geofoam in reducing earth pressure on retaining structures under dynamic loading. *Int J Geosynth Ground Eng*. <https://doi.org/10.1007/s40891-021-00304-8>
10. Henriques IR, Rouleau L, Castello DA et al (2020) Viscoelastic behavior of polymeric foams: experiments and modeling. *Mech Mater* 148:103506. <https://doi.org/10.1016/j.mechmat.2020.103506>
11. Rastegar N, Ershad-Langroudi A, Parsimehr H, Moradi G (2022) Sound-absorbing porous materials: a review on polyurethane-based foams. *Iran Polym J* 31:83–105. <https://doi.org/10.1007/s13726-021-01006-8>
12. Al Rifaie M, Abdulhadi H, Mian A (2022) Advances in mechanical metamaterials for vibration isolation: a review. *Adv Mech Eng* 14:168781322210828. <https://doi.org/10.1177/16878132221082872>
13. Liyanapathirana DS, Ekanayake SD (2016) Application of EPS geofoam in attenuating ground vibrations during vibratory pile driving. *Geotext Geomembr* 44:59–69. <https://doi.org/10.1016/j.geotextmem.2015.06.007>
14. Jelle BP (2011) Traditional, state-of-the-art and future thermal building insulation materials and solutions – properties, requirements and possibilities. *Energy Build* 43:2549–2563. <https://doi.org/10.1016/j.enbuild.2011.05.015>
15. Liu S, Duvigneau J, Vancso GJ (2015) Nanocellular polymer foams as promising high performance thermal insulation materials. *Eur Polym J* 65:33–45. <https://doi.org/10.1016/j.eurpolymj.2015.01.039>
16. Wang G, Zhao J, Wang G et al (2017) Low-density and structure-tunable microcellular PMMA foams with improved thermal-insulation and compressive mechanical properties. *Eur Polym J* 95:382–393. <https://doi.org/10.1016/j.eurpolymj.2017.08.025>
17. ASTM D6817 (2021) Specification for rigid cellular polystyrene geofoam [D35 Committee]. ASTM International
18. Global Market Insights Geofoam Market - By product (EPS Geofoam, XPS Geofoam), by application (Void fill, slope stabilization, embankments, retaining structures, insulation, and others), by end use (Road & railways, building & construction), & Global Forecast, 2023–2032
19. Stark TD, Arellano D, Horvath JS, Leshchinsky D (2004) Geofoam applications in the design and construction of highway embankments. Transportation Research Board, Washington, D.C.
20. ASTM 7180 (2021) Guide for use of expanded polystyrene (EPS) geofoam in geotechnical Projects [D35 Committee]. ASTM International
21. Negussey D (2007) Design parameters for EPS geofoam. *Soils Found* 47:161–170. <https://doi.org/10.3208/sandf.47.161>
22. Leo CJ, Kumruzzaman M, Wong H, Yin JH (2008) Behavior of EPS geofoam in true triaxial compression tests. *Geotext Geomembr* 26:175–180. <https://doi.org/10.1016/j.geotextmem.2007.10.005>
23. Beju YZ, Mandal JN (2017) Expanded polystyrene (EPS) geofoam: preliminary characteristic evaluation. *Procedia Eng* 189:239–246. <https://doi.org/10.1016/j.proeng.2017.05.038>
24. Ossa A, Romo MP (2009) Micro- and macro-mechanical study of compressive behavior of expanded polystyrene geofoam. *Geosynth Int* 16:327–338. <https://doi.org/10.1680/gein.2009.16.5.327>
25. Malai A, Youwai S (2021) Stiffness of expanded polystyrene foam for different stress states. *Int J Geosynth Ground Eng*. <https://doi.org/10.1007/s40891-021-00321-7>
26. Atmatzidis DK, Missirlis EG, Chrysikos DA (2001) An investigation of EPS geofoam behavior in compression. 2001 Third international conference on EPS–EPS geofoam. Salt Lake City, USA, pp 1–11
27. Trandafir AC, Bartlett SF, Lingwall BN (2010) Behavior of EPS geofoam in stress-controlled cyclic uniaxial tests. *Geotext Geomembr* 28:514–524. <https://doi.org/10.1016/j.geotextmem.2010.01.002>
28. Sreekantan PG, Ramana GV (2023) Roughness based prediction of geofoam interfaces with concrete. *Geosynthetics: leading the way to a resilient planet*, 1st edn. CRC Press, London, pp 580–585
29. Sreekantan PG, Ramana GV, Nohawar PS (2023) Assessing the flexural characteristics of geofoam using digital image correlation technique. *IJEMS*. <https://doi.org/10.56042/ijems.v30i4.642>
30. Elragi A, Negussey D, Kyanka G (2001) Sample size effects on the behavior of EPS geofoam. In: *Soft ground technology*. American Society of Civil Engineers, Noordwijkerhout, The Netherlands, pp 280–291
31. Abdelrahman GE, Kawabe S, Tatsuoaka F, Tsukamoto Y (2008) Rate effects on the stress-strain behaviour of eps geofoam. *Soils Found* 48:479–494. <https://doi.org/10.3208/sandf.48.479>
32. Cronin DS, Ouellet S (2016) Low density polyethylene, expanded polystyrene and expanded polypropylene: strain rate and size effects on mechanical properties. *Polym Test* 53:40–50. <https://doi.org/10.1016/j.polymertesting.2016.04.018>
33. Mohamed G, Hegazy R, Mohamed M (2017) An investigation on the mechanical behavior of expanded polystyrene (EPS) geofoam under different loading conditions. *Int J Plast Technol* 21:123–129. <https://doi.org/10.1007/s12588-017-9175-6>
34. Khalaj O, Mohammad Amin Ghotbi Siabil S, Naser Moghaddas Tafreshi S et al (2020) The experimental investigation of behaviour of expanded polystyrene (EPS). *IOP Conf Ser: Mater Sci Eng* 723:012014. <https://doi.org/10.1088/1757-899X/723/1/012014>
35. Del Rosso S, Iannucci L (2020) On the compressive response of polymeric cellular materials. *Materials*. <https://doi.org/10.3390/ma13020457>
36. Žiliūtė L, Motiejūnas A, Kleizienė R et al (2016) Temperature and moisture variation in pavement structures of the test road. *Transp Res Procedia* 14:778–786. <https://doi.org/10.1016/j.trpro.2016.05.067>
37. Murari KK, Ghosh S, Patwardhan A et al (2015) Intensification of future severe heat waves in India and their effect on heat stress and mortality. *Reg Environ Change* 15:569–579. <https://doi.org/10.1007/s10113-014-0660-6>
38. Zou Y, Leo CJ (2001) Compressive behaviour of eps geofoam at elevated temperatures. In: 3rd international conference on EPS geofoam, EPS 2001



39. Krundaeva A, De Bruyne G, Gagliardi F, Van Paepegem W (2016) Dynamic compressive strength and crushing properties of expanded polystyrene foam for different strain rates and different temperatures. *Polym Testing* 55:61–68. <https://doi.org/10.1016/j.polymertesting.2016.08.005>
40. Jayawardana P, Thambiratnam DP, Perera N et al (2019) Use of artificial neural network to evaluate the vibration mitigation performance of geofoam-filled trenches. *Soils Found* 59:874–887. <https://doi.org/10.1016/j.sandf.2019.03.004>
41. Rodríguez-Sánchez AE, Plascencia-Mora H (2022) A machine learning approach to estimate the strain energy absorption in expanded polystyrene foams. *J Cell Plast* 58:399–427. <https://doi.org/10.1177/0021955X211021014>
42. Rodríguez-Sánchez AE, Plascencia-Mora H (2023) Modeling hysteresis in expanded polystyrene foams under compressive loads using feed-forward neural networks. *J Cell Plast*. <https://doi.org/10.1177/0021955X231174362>
43. Akis E, Guven G, Lotfisadigh B (2022) Predictive models for mechanical properties of expanded polystyrene (EPS) geofoam using regression analysis and artificial neural networks. *Neural Comput Appl* 34:10845–10884. <https://doi.org/10.1007/s00521-022-07014-w>
44. Pant A, Ramana GV (2022) Prediction of pullout interaction coefficient of geogrids by extreme gradient boosting model. *Geotext Geomembr* 50:1188–1198. <https://doi.org/10.1016/j.geotextmem.2022.08.003>
45. Feng D-C, Wang W-J, Mangalathu S et al (2021) Implementing ensemble learning methods to predict the shear strength of RC deep beams with/without web reinforcements. *Eng Struct* 235:111979. <https://doi.org/10.1016/j.engstruct.2021.111979>
46. ASTM D1622 (2020) Test method for apparent density of rigid cellular plastics [D20 Committee]. ASTM International
47. ASTM D1621–16 (2023) Test method for compressive properties of rigid cellular plastics [D20 Committee]. ASTM International
48. Sreekantan PG, Vangla P, Ramana GV (2023) Image-aided physical and compression characterisation of expanded polystyrene geofoam. *Geosynth Int*. <https://doi.org/10.1680/jgein.22.00363>
49. Likitlersuang S, Teachavorasinskun S, Surarak C et al (2013) Small strain stiffness and stiffness degradation curve of Bangkok Clays. *Soils Found* 53:498–509. <https://doi.org/10.1016/j.sandf.2013.06.003>
50. Gibson LJ, Ashby MF (1997) Cellular solids: structure and properties, 2nd edn. Cambridge University Press, Cambridge
51. Momanyi J, Herzog M, Muchiri P (2019) Analysis of thermomechanical properties of selected class of recycled thermoplastic materials based on their applications. *Recycling* 4:33. <https://doi.org/10.3390/recycling4030033>
52. Kang W-J, Cheon S-S, Lee I-H et al (2010) Investigation of the strain rate effects of EPS foam. *J Korean Soc Compos Mater* 23:64–68. <https://doi.org/10.7234/kscm.2010.23.3.064>
53. Li Z, Gao X, Lu D (2021) Correlation analysis and statistical assessment of early hydration characteristics and compressive strength for multi-composite cement paste. *Constr Build Mater* 310:125260. <https://doi.org/10.1016/j.conbuildmat.2021.125260>
54. Chan YH (2003) Biostatistics 104: correlational analysis. *Singap Med J* 44:614–619
55. Dantas SA, Rafiq SK, Ahmed HU et al (2023) Innovative soft computing techniques including artificial neural network and nonlinear regression models to predict the compressive strength of environmentally friendly concrete incorporating waste glass powder. *Innov Infrastruct Solut* 8:119. <https://doi.org/10.1007/s41062-023-01089-7>
56. Dantas ATA, Batista Leite M, De Jesus NK (2013) Prediction of compressive strength of concrete containing construction and demolition waste using artificial neural networks. *Constr Build Mater* 38:717–722. <https://doi.org/10.1016/j.conbuildmat.2012.09.026>
57. Ebdali M, Khorasani E, Salehin S (2020) A comparative study of various hybrid neural networks and regression analysis to predict unconfined compressive strength of travertine. *Innov Infrastruct Solut* 5:93. <https://doi.org/10.1007/s41062-020-00346-3>
58. Duan J, Asteris PG, Nguyen H et al (2021) A novel artificial intelligence technique to predict compressive strength of recycled aggregate concrete using ICA-XGBoost model. *Eng Comput* 37:3329–3346. <https://doi.org/10.1007/s00366-020-01003-0>
59. Nguyen N-H, Abellán-García J, Lee S et al (2022) Efficient estimating compressive strength of ultra-high performance concrete using XGBoost model. *J Build Eng* 52:104302. <https://doi.org/10.1016/j.jobe.2022.104302>
60. Uddin MN, Li L-Z, Deng B-Y, Ye J (2023) Interpretable XGBoost–SHAP machine learning technique to predict the compressive strength of environment-friendly rice husk ash concrete. *Innov Infrastruct Solut* 8:147. <https://doi.org/10.1007/s41062-023-01122-9>
61. Huu Nguyen M, Nguyen T-A, Ly H-B (2023) Ensemble XGBoost schemes for improved compressive strength prediction of UHPC. *Structures* 57:105062. <https://doi.org/10.1016/j.istruc.2023.105062>
62. Haykin S (2009) Neural networks and learning machines, 3/E. Pearson Education India, Noida
63. Abu-Mostafa YS (1995) Hints. *Neural Comput* 7:639–671
64. Alwosheel A, Van Cranenburgh S, Chorus CG (2018) Is your dataset big enough? Sample size requirements when using artificial neural networks for discrete choice analysis. *J Choice Model* 28:167–182. <https://doi.org/10.1016/j.jocm.2018.07.002>
65. Mihlayanlar E, Dilmaç Ş, Güner A (2008) Analysis of the effect of production process parameters and density of expanded polystyrene insulation boards on mechanical properties and thermal conductivity. *Mater Des* 29:344–352. <https://doi.org/10.1016/j.matdes.2007.01.032>
66. Yan S, Wang Y, Wang D, He S (2022) Application of EPS geofoam in rockfall galleries: insights from large-scale experiments and FDEM simulations. *Geotext Geomembr* 50:677–693. <https://doi.org/10.1016/j.geotextmem.2022.03.009>
67. Horvath JS (1994) Expanded polystyrene (EPS) geofoam: an introduction to material behavior. *Geotext Geomembr* 13:263–280. [https://doi.org/10.1016/0266-1144\(94\)90048-5](https://doi.org/10.1016/0266-1144(94)90048-5)
68. Duskov M (1997) Materials research on EPS20 and EPS15 under representative conditions in pavement structures. *Geotext Geomembr* 15:147–181. [https://doi.org/10.1016/S0266-1144\(97\)00011-3](https://doi.org/10.1016/S0266-1144(97)00011-3)
69. Aleksander I, Morton H (1990) An introduction neural computing. Chapman and Hall, London
70. Agatonovic-Kustrin S, Beresford R (2000) Basic concepts of artificial neural network (ANN) modeling and its application in pharmaceutical research. *J Pharm Biomed Anal* 22:717–727. [https://doi.org/10.1016/S0731-7085\(99\)00272-1](https://doi.org/10.1016/S0731-7085(99)00272-1)
71. Erzin Y, Rao BH, Patel A et al (2010) Artificial neural network models for predicting electrical resistivity of soils from their thermal resistivity. *Int J Therm Sci* 49:118–130. <https://doi.org/10.1016/j.ijthermalsci.2009.06.008>
72. Moradi MJ, Khaleghi M, Salimi J et al (2021) Predicting the compressive strength of concrete containing metakaolin with different properties using ANN. *Measurement* 183:109790. <https://doi.org/10.1016/j.measurement.2021.109790>
73. Lin C-J, Wu N-J (2021) An ANN model for predicting the compressive strength of concrete. *Appl Sci* 11:3798. <https://doi.org/10.3390/app11093798>
74. Eskandari-Naddaf H, Kazemi R (2017) ANN prediction of cement mortar compressive strength, influence of cement strength class.



- Constr Build Mater 138:1–11. <https://doi.org/10.1016/j.conbuildmat.2017.01.132>
75. Chen T, Guestrin C (2016) XGBoost: a scalable tree boosting system. In: Proceedings of the 22nd ACM SIGKDD international conference on knowledge discovery and data mining. ACM, San Francisco California USA, pp 785–794
  76. Nguyen HD, Truong GT, Shin M (2021) Development of extreme gradient boosting model for prediction of punching shear resistance of r/c interior slabs. Eng Struct 235:112067. <https://doi.org/10.1016/j.engstruct.2021.112067>
  77. Rathakrishnan V, Bt. Beddu S, Ahmed AN (2022) Predicting compressive strength of high-performance concrete with high volume ground granulated blast-furnace slag replacement using boosting machine learning algorithms. Sci Rep 12:1–16. <https://doi.org/10.1038/s41598-022-12890-2>
  78. Pedregosa F, Varoquaux G, Gramfort A et al (2011) Scikit-learn: Machine learning in Python. J Mach Learn Res 12:2825–2830
  79. Feng D-C, Liu Z-T, Wang X-D et al (2020) Machine learning-based compressive strength prediction for concrete: an adaptive boosting approach. Constr Build Mater 230:117000. <https://doi.org/10.1016/j.conbuildmat.2019.117000>
  80. Han Q, Gui C, Xu J, Lacidogna G (2019) A generalized method to predict the compressive strength of high-performance concrete by improved random forest algorithm. Constr Build Mater 226:734–742. <https://doi.org/10.1016/j.conbuildmat.2019.07.315>

Springer Nature or its licensor (e.g. a society or other partner) holds exclusive rights to this article under a publishing agreement with the author(s) or other rightsholder(s); author self-archiving of the accepted manuscript version of this article is solely governed by the terms of such publishing agreement and applicable law.